Journal of Engineering Science and Technology
Vol. 13, No. 11 (2018) 3874 - 3893

SCATTERING EFFECTS BY SiO_2 NANO-MICROPARTICLE AND FREE SPACE ATTENUATION MODELLING FOR DIVERSE WEATHER CONDITIONS

ADIB K. CHOWDHURY*, MAMUN B. I. REAZ

Department of Electrical, Electronic and Systems Engineering,
National University of Malaysia, 43600, Bangi, Selangor Darul Ehsan, Malaysia
*Corresponding Author: chowdhury_adib@yahoo.com

Abstract

This article presents few empirical models to be used prediction of atmospheric attenuation due to airborne suspended particles such as sand, dust, fog and mist. The attenuation can be determined using the proposed models as standard methods considering various types of weather conditions including silica-dominant sandstorm, dust storm, fog or mist. As atmospheric attenuation heavily affects the transmission of data using visible light communication, we study the effect of air suspended particles to scattering amplitude and turbulence phase of the light beam. The proposed models are compared with existing attenuation models in the case of attenuation under foggy weather condition. The proposed models especially proposed Model 2 is seen to be best fit for prediction of atmospheric attenuation under dense to very light fog weather.

Keywords: Atmospheric attenuation, Fog attenuation, Dust and sandstorm, Visibility, Visible light communication.

1. Introduction

Wireless communication has been widely integrated into our daily lives. With the increasing use of mobile peripherals and other devices, congestion of communication to Radio Frequency (RF) has worsened due to the demand for wireless data. There are few alternatives to overcome the congestion to the traditional RF with one of them being the optical wireless communication (OWC). Interestingly, this technology particularly the visible light-based communication is a viable and cheaper alternative to RF with its capability to offer a wider range of spectrum to be used in data communication. O'Brien et al. (2003) explained that visible light communication (VLC) is a system consisting of a device for transmission to modulate the LED illumination intensity, air as its propagation channel and photodiode as the receiver [1]. This system is sometimes referred to as Light Fidelity or as Li-Fi [1]. The wide availability of light emitting diodes (LEDs) exploited in various industries around the world currently makes it possible to use them as both lighting and communication medium. This instantaneous dual usage of LEDs leads to the use of data communication aspect at a very low cost [2]. The variation to the intensity of LEDs that makes data communication possible is undetected by human eyes. Hence, communication of different data can be done between visible light and light-sensitive receiver [3-5].

According to Harb et al. [6], variations of weather conditions such as rain, snow, fog, mist, sand and dust storms strongly affect the communication signals' propagation. The severity of this disturbance heavily depended on the weather conditions. In the case of RF communication using satellite, a normal dust storm will lead to attenuation. However, if an intense dust storm is to occur, this may result in the loss of satellite link [6]. As reported by Harb et al. [7], consequently, stark weather conditions can heavily reduce the performance of wireless communication systems. According to Alhaider [8], the visibility observed during dust and sand storms can range from 10 kilometres to only a few metres. Signal attenuation occurring because of the presence fog, mist, dust and sandstorm are one of the many possible problems and challenges that need to be addressed so that reliable wireless communication services can be provided. Similar to the RF technology, visible light communication is also susceptible to attenuation caused by weather-related factors. According to Ijaz et al. [9], the atmospheric constituents particularly the air-suspended colloid of fine particles such as fog, smoke and dust have sizes comparable to the size distributions of optical wavelengths in free space optics (FSO). As a result, degradation of the performance and availability of FSO link can happen due to the affected scattering and absorption of the optical light [10, 11]. Apart from these, the interaction between the turbulent channel and optical light in the atmosphere also reduces the strength of the transmitted signal [12]. Many researchers did focusing on attenuation/path loss modelling. However, most of them give focus to the infra-red (IR) based wireless communications [13, 14].

The transport of wind-blown sand and dust particles is a potent natural force, which contributes to a significant portion of the Earth's atmosphere. According to Kok et al. [15], the transportation of sand particles predominantly depends on the inherent weather and particle size. These inorganic mineral particles have diameters, d between 62.5 to 2,000 μm [16]. As wind speed increases, sand particles of $d \cong 100\ \mu m$ are the first to be moved by fluid drag. Numerous studies indicate the vital constituent of the sand particle to be silica SiO_2 in the form of quartz. Quantitative analysis of sand samples from Illinois, United States of America and Zauma River, Nigeria show that SiO_2 constituent of sand is observed

to be 87.91% and 81.5% respectively [17]. Only the dominant silica content of sand storm is taken into consideration for detailed analysis to demonstrate the effect of sand to atmospheric attenuation. Similar approach can be done to predict attenuation affected by suspended water globules present in fog. Due to the similarities of diameter sizes and the comparable refraction index of SiO_2 and water particles, the standard empirical method can be developing to exhibit the atmospheric attenuation due to fog, sand and dust.

In this research work, we propose few standardize empirical models to observe atmospheric attenuation affected by dust, sand and fog. Visibility data obtained from the historical record of global weather stations and airports by National Oceanic and Atmospheric Administration (NOAA) are broadly utilised to demonstrate the empirical models. Here, we predict the sand, dust and fog effects on free space communication particularly VLC. The only parameter that we consider in determining this model is visibility affected by the airborne particles particularly dust, silica-dominant sand and fog. For a corresponding particle, the parameters pragmatic considerations that are taken into account are the diameter of particles and their photonics properties including wavelength. This paper is organised as follows: a presentation of existing optical beam induced atmospheric attenuation models are made in Section 2 followed by a few newly proposed attenuations models in Section 3. In Section 4, observations on the effects of atmospheric dust and sand particles to turbulence induced phase and scattering amplitude are thoroughly discussed. Section 5 shows the comparison and discussion of existing attenuation models with the proposed empirical model considering suspended water globules in fog as case analysis. The paper ends with conclusions drawn in Section 6.

2. Optical Beam Induced Atmospheric Attenuation Models

The complex and dynamic atmospheric channel affects the features of propagating optical beam; triggering turbulence-induced optical loss and phase fluctuations. Propagating optical signal in free space channel is sensitive to atmospheric airborne micro-nano particles such as sand (SiO_2), dust, fog, dirt, rain, smoke, mist etc. Such inhalable coarse and fine particles are a mixture of solid particles and liquid droplets. A typical open field air sample indicates SiO_2 particle size variation ranging from 0.5 nm to 180 µm. Atmospheric particle scattering induces signal degradation and noise injection in a free-space optical communication system. Furthermore, chronological and spatial signal attenuation can be observed as particle concentration fluctuates in the atmosphere. In this section, we discuss and present the existing models on optical beam induced atmospheric attenuation. The atmospheric attenuation coefficient $\beta_\lambda(\upsilon)$ and transmission path length L_T are presented by the Beer-Lambert's law as [18],

$$T_O(\lambda, L_T) = \frac{P_R}{P_T} = e^{-\beta_A(\lambda) \times L_T} \quad (1)$$

Methods where optical power at receiver P_R, transmitted power P_T, optical depth τ_{0d} and attenuation coefficient $\beta_A(\lambda)$ represent the total optical transmittance $T_O(\lambda, L_T)$ at wavelength λ. The optical transmittance $T_O = e^{-\tau_{Od}}$ is the fraction of transmitted power. The transmitted power is related to the receiver power by $P_R = P_T g e^{-\tau_{Od}}$. The airborne particles collide with propagating optical beam creating absorption and scattering effects. The atmospheric aerosol is composed of nanoparticles ranging from spherical to irregular in shapes. According to Ghassemlooy et al. [19], a general atmospheric attenuation coefficient can be expressed as,

$$\beta_A(\lambda)=\mathrm{Abs}_{\mathrm{mol}}(\lambda)+\mathrm{Abs}_{\mathrm{Aeo}}(\lambda)+\mathrm{Scat}_{\mathrm{mol}}(\lambda)+\mathrm{Scat}_{\mathrm{Aeo}}(\lambda) \quad (2)$$

where the molecular and aerosol absorption coefficient is presented by $\mathrm{Abs}_{\mathrm{mol}}(\lambda)$ and $\mathrm{Abs}_{\mathrm{Aeo}}(\lambda)$, respectively. Similarly, scattering coefficients for molecular and aerosol particles are denoted by $\mathrm{Scat}_{\mathrm{mol}}(\lambda)$and $\mathrm{Scant}_{\mathrm{Aeo}}(\lambda)$.

Complex process of light scattering and absorption by atmospheric particles involves theoretical and mathematical elaboration. Structure size and incident light beam's photonic wavelength $\boldsymbol{\lambda}$ play crucial role in determining regional scattering process. As commented by Behrend and Huffman [20], Mie scattering is observed for haze and fog particles boundary when wavelength is at $0.05\mu m \leq \lambda \leq 20\mu m$. Airborne coastal SiO_2 structure exhibits similar size distribution. Theoretical and empirical Mie-induced attenuation models for similar spherical structures are widely observed in FSO systems. The cross-sections of the particle can be denoted by scattering $C_{\mathrm{Scat}}=\mathrm{P}_{\mathrm{Scat}}/\mathrm{I}_O a$ or absorption $C_{\mathrm{Abs}}=\mathrm{P}_{\mathrm{Abs}}/\mathrm{I}_O$, where P_{Scat} and P_{Abs} are the scattered and absorbed electromagnetic energy across an imaginary surface of sphere, respectively. The incident optical radiation exhibit intensity I_O in W/m^2. According to Ijaz et al. [21], the theoretical normalized scattering efficiency Q_{Scat} can be estimated.

$$Q_{\mathrm{Scat}} = \frac{C_{\mathrm{Scat}}}{\pi \mathrm{r}_S^2} \quad (3)$$

where r_s is the structure radii and unitless parametrical function Q_{Scat}. The atmospheric attenuation coefficient $\beta_A(\lambda)$ is estimated based on structural and optical assumptions [18]. Independent structures are assumed to be spherical with a complex refractive index of $\mathrm{n}=\mathrm{n}_r\text{-}jn_i$. Weichel [22] presented the attenuation coefficient $\beta_A(\lambda)$ of the scattered optical signal.

$$\beta_A(\lambda)=\pi r_s^2 \int_0^{\infty} Q_{\mathrm{Scat}}\left(\frac{2\pi r_S}{\lambda},\mathrm{n}_r\right) \quad N(r_s)\mathrm{d}r_s \quad (4)$$

where the real part of the complex refractive index is n_r, the imaginary part n_i represents absorption, volume concentration is denoted by $N(r_s)$. Subsequently, absorption specific attenuation is defined by $\beta_A=\mathrm{C}_l\times\lambda^{-\mu}$. borne and Huffman [20] presented the visual range parameters $C_l$and μ are related to visual V by Kim's model.

$$C_l = \frac{3.91}{V}(\lambda_R)^{\mu}; \qquad \lambda_R@550\ \mathrm{nm} \quad (5)$$

According to Kruse et al. [23], the structure size distribution function $N(r_s)$ is represented by analytical functions for fog or haze like atmospheric constituents such as SiO_2 particle.

$$N(r_s)=\mathrm{a}r_s^{\alpha}e^{(-\beta \mathrm{r}_S)} \quad (6)$$

where a, α and β are the parameters characterize the structural size distribution. The optical attenuation due to such atmospheric condition depends on multiple factors such as transmitter location, structure size distribution and average particle diameter. Therefore, predicting attenuation becomes challenging due to location varying structural concentration in atmosphere. Due to complexity in particle physical property and unavailability of size distribution, similar particle induced optical signal attenuation can be predicted using empirical models [24, 25]. As presented by Grabner and Kvicera [24], the meteorological visibility υ and attenuation $\beta_\lambda(\upsilon)$ is utilized by the empirical relationship.

$$\beta_\lambda(\upsilon) = \frac{10 \cdot log_{10}(\tau)}{\upsilon(km)} \cdot \left(\frac{\lambda}{\lambda_R}\right)^{-\mu} \quad (7)$$

where meteorological visibility $\boldsymbol{\upsilon}$expressed as $\upsilon = 10 \cdot \log(\tau)\,/\beta_\lambda$, incident beam wavelength is denoted as λ, maximum solar band spectrum λ_R and Koschmieder transmittance threshold T_{th} is set as 2%. However, considering aeronautical requirements T_{th} can be set as 5%. μ is the particle size distribution related coefficient and corresponding values are provided as:

$$\mu = \begin{cases} 1.6 & for \quad \upsilon > 50 \text{ km} \\ 1.3 & for 6 \text{ km} < \upsilon < 50 \text{ km} \\ 0.585\upsilon^{1/3} & for\ 0 \text{ km} < \upsilon < 6 \text{ km} \end{cases} \quad (8)$$

Investigation on specific empirical data region indicates that attenuation $\beta_\lambda(\upsilon)$ is wavelength independent. Kim model elaborates on this concept and defines values of μ as,

$$\mu = \begin{cases} 1.6 & for & \upsilon > 50 & \text{km} \\ 1.3 & for & 6 < \upsilon < 50 & \text{km} \\ 0.16\upsilon + 0.34 & for & 1 < \upsilon < 6 & \text{km} \\ \upsilon - 0.5 & for & 0.5 < \upsilon < 1 & \text{km} \\ 0 & for & \upsilon < 0.5 & \text{km} \end{cases} \quad (9)$$

It is reported by Ijaz et al. [21] that Kim's model is deduced from Kruse model by utilizing theoretical assumptions on particle size distribution coefficient. The μ values indicate that $\beta_\lambda(\upsilon)$ is wavelength independent for visibility < 0.5 km. Contrariwise, Al-Naboulsi proposed an advection-convection fog attenuation model for $\upsilon \cong (0.05 \text{ km} - 1 \text{ km})$. The mathematical models are shown as below,

$$\alpha_{con}(\lambda) = 10 \cdot \log_e\left(\frac{0.11478\lambda + 3.8367}{\upsilon}\right) \quad (10)$$

$$\alpha_{adv}(\lambda) = 10 \cdot \log_e\left(\frac{0.18126\lambda^2 + 0.13709\lambda + 3.7205}{\upsilon}\right) \quad (11)$$

Weather, location, particle distribution and atmospheric factor-dependent nature of empirical model poses an immense challenge to secure a standard platform for optical attenuation modelling. However, experimental and theoretical estimations indicate that incident photonic wavelength functions as an active stimulator for scattering and absorption process.

3. Proposed Attenuation Models

Due to construction, mining and wind movement, the airborne respirable crystalline SiO_2 particles are found perennially in urban, suburban, rural and exurban communities. With approaching similarities in diameter size and refraction index of SiO_2 particles and the water particles in fog, a standard procedure in predicting attenuation can be applied. Therefore, the proposed model emphasizes on visibility measurement υ and optical beam wavelength λ_{nm}. Based on the analysis by Duvey and Gupta [26], it is observed that as υ reduces for any incident λ_{nm}, the values of μ can be obtained by $0.2\,\upsilon$. A μ buffer zone is introduced for region $20\ km \leq \upsilon < 50\ km$ to investigate airborne particles of $0.5\ nm < d < 100\ \mu m$ in clear atmospheric conditions. Few models are proposed for the prediction of attenuation due to SiO_2, fog and smoke like particle movement in atmosphere. The particle size related coefficient μ for proposed Model 3 and 4 can be presented by:

$$\mu = \begin{cases} 1.6 & for \quad \upsilon \geq 50 \quad \text{km} \\ 1.5 & for 20 \leq \upsilon < 50 \text{ km} \\ 1.15 & for\ 2 \leq \upsilon < 20 \ \text{km} \\ 0.16\upsilon + 0.34 & for\ \ 1 \leq \upsilon < 2 \ \ \text{km} \\ \upsilon - 0.5 & for\ 0.5 \leq \upsilon < 1 \ \text{km} \\ 0.2\upsilon & for\ 0 < \upsilon < 0.5 \ \text{km} \end{cases} \tag{12}$$

The visibility is expressed in terms of atmospheric turbulence. As the incident light propagates through the atmospheric turbulence, ν, the attenuation is observed as the turbulence derivative of optical power P. The attenuation is considered to be a scalar physical quantity. Proposed Model 3 is expressed as,

$$\beta_\lambda(\upsilon) = \frac{\delta P}{\delta \upsilon} = \frac{\delta}{\delta \upsilon}\gamma(\upsilon) = \left[\frac{3.912 - 10\, log_{10}(\tau)}{2\upsilon}\right] \times \left(\frac{\lambda_{nm}}{\lambda_R}\right)^{-\mu} \tag{13}$$

It is observed that Proposed 4 partially operates in the visibility range of $20 \text{ km} \leq \upsilon < 50 \text{ km}$. The attenuation indicates a varying wavelength of $350 \text{ nm} < \lambda_{nm} < 1500 \text{ nm}$ for thick to light atmospheric condition of $0.05\ km \leq \upsilon < 1\ km$. The model is presented by equation below:

$$\beta_\lambda(\upsilon) = \frac{9}{50} + \left[\frac{3.912 - 10\, log_{10}(\tau)}{2(\upsilon - 3)}\right] \cdot \left(\frac{\lambda_{nm}}{\lambda_R}\right)^{-\mu} \tag{14}$$

Optical power $\gamma(\nu)$ represents the intermittent signal strength between the beam transmitter and receiving plane. The optical power is expressed in dB and given by,

$$\gamma(\upsilon) = \int \beta_\lambda(\upsilon)\delta\upsilon = \frac{9}{50}\upsilon + log_e(\upsilon - 3) \cdot [1.956 - 5\, log_{10}(\tau)] \cdot \left(\frac{\lambda_{nm}}{\lambda_o}\right)^{-\mu} \tag{15}$$

Psi attenuation is defined as the rate of change of signal attenuation with respect to atmospheric turbulence. An average psi attenuation $\psi'(\upsilon)$ over a period of turbulence is denoted by $\frac{\delta \beta_\lambda(\upsilon)}{\delta \upsilon}$ and expressed as,

$$\frac{\delta}{\delta \upsilon}\psi(\upsilon) = \psi'(\upsilon) = \frac{\delta}{\delta \upsilon}\beta_\lambda(\upsilon) \tag{16}$$

where visibility υ is presented in distance km. High visibility interprets low atmospheric turbulence while low visibility indicates high turbulence. The psi attenuation of the Proposed 4 model is expressed by,

$$\psi(\upsilon) = \frac{\delta}{\delta \upsilon}\beta_\lambda(\upsilon) = \left[\frac{5\, log_{10}(\tau) - 1.956}{(\upsilon - 3)^2}\right] \cdot \left(\frac{\lambda_{nm}}{\lambda_o}\right)^{-\mu} \tag{17}$$

The period of turbulence is observed by the visibility measurements. The historical visibility data is obtained by NOAA from most global weather stations and airports for many years [27]. Nature of physical scattering and wavelength λ_{nm} dependency of attenuation $\beta(\upsilon)$ is closely observed by coefficient μ. Based on theoretical assumptions values of μ are proposed for Model 1 and 2 shown as,

$$\mu = \begin{cases} 1.6 & for \quad \upsilon \geq 50 \quad \text{km} \\ 1.15 & for 20 \leq \upsilon < 50 \text{ km} \\ 1.3 & for\ 2 \leq \upsilon < 20 \ \text{km} \\ 0.16\upsilon + 0.34 & for\ \ 1 \leq \upsilon < 2 \ \ \text{km} \\ \upsilon - 0.5 & for\ 0.5 \leq \upsilon < 1 \ \text{km} \\ 0 & for\ 0 < \upsilon < 0.5 \ \text{km} \end{cases} \tag{18}$$

It is observed that Proposed 2 exhibit similar behaviour for visibility $v \cong (2\text{ km} - 3\text{ km})$. Optical signal attenuation, power and psi attenuation is presented in Eqs. (19) to (21) respectively. Different models are also utilized for viability prediction against measured visibility data. Proposed and curve fitting models are presented in Table 1.

$$\beta_\lambda(v) = -\left[\frac{5\log_{10}(T^{th})}{v}\right] \cdot \left(1 + \frac{\lambda_{nm}}{\lambda_o}\right)^{-\mu} \tag{19}$$

$$\gamma(v) = -5\log_{10}(T^{th}) \cdot log_e(v) \cdot \left(1 + \frac{\lambda_{nm}}{\lambda_o}\right)^{-\mu} \tag{20}$$

$$\psi(v) = \left[\frac{5\log_{10}(T^{th})}{v^2}\right] \cdot \left(1 + \frac{\lambda_{nm}}{\lambda_o}\right)^{-\mu} \tag{21}$$

The meteorological channel visibility range is utilized to understand the behaviour of particle attenuation. The aeronautical consideration for $\tau = 0.05$ is adopted as opposed to Koshmieder law. The $\beta_\lambda(v)$ is expressed in dB/km, mathematically defined by wavelength λ_{nm} (350 nm – 1500 nm), reference wavelength λ_o (550 nm) and transmittance τ.

Table 1. Proposed and curve fitting mathematical models based on incident wavelength and visibility.

Parameter	Proposed 1	Power	Logarithm	Polynomial
$\beta_\lambda(v)$	$\frac{1}{v} \cdot \begin{pmatrix} 1.956\left(\frac{\lambda_{nm}}{\lambda_o}\right)^{-\mu} \\ -5\,log_{10}(T^{th}) \end{pmatrix}$	$13.086v^{-1.4}$	$-0.821 \cdot log_e(v) + 3.134$	$\frac{1}{1000} \cdot \begin{bmatrix} 2v^2 - 1160v \\ +2293 \end{bmatrix}$
$\gamma(v)$	$log(v) \cdot \begin{pmatrix} 1.956\left(\frac{\lambda_{nm}}{\lambda_o}\right)^{-\mu} \\ -5\,log_{10}(T^{th}) \end{pmatrix}$	$5.437v^{2.407}$	$-0.821v \cdot log_e(v) + 3.955v$	$\frac{2v^3}{3000} - \frac{58v^2}{1000} + \frac{2293v}{1000}$
$\psi(v)$	$-\frac{1}{v^2} \cdot \begin{pmatrix} 1.956\left(\frac{\lambda_{nm}}{\lambda_o}\right)^{-\mu} \\ -5\,log_{10}(T^{th}) \end{pmatrix}$	$18.412v^{0.40}$	$-\frac{0.821}{v}$	$0.004\,v - 0.116$

4. Turbulence Induced Phase and Scattering Amplitude Fluctuation

The light scattering is heavily affected by the atmospheric particles. In this section, we discuss how suspended atmospheric particles resulting in fluctuations of light scattering amplitude and turbulence. It is observed that the transmitted light beam I_o heavily interacts with the atmospheric particles in free space. At this point, incident light wavelength λ_{nm}, particle size in diameter d and its optical properties relative to transport medium exhibits an important role on the scattering effect. The obtained silica SiO_2 and dust particle samples range from size d ≈ 805 nm-316 μm.

Particle shape is considered to be spherical. It provides the largest radius r or diameter d to find the dimensionless size parameter. It is observed that the particle size is slightly larger than the incident light wavelength. Therefore, Mie scattering theory is utilized to observe the spherical scattering without any particular limit set

on the particle size. Mie scattering relates to the properties of the light photons with respect to atmospheric turbulence when it encounters different size of transmission medium particles. The collision causes the light beam to experience different scattering paradigms.

Mie scattering geometry calculates the scattered electromagnetic field of the homogeneous transmission medium and internal SiO_2 particle. Therefore, scattering observation is achieved in the far and near field zones. Complex scattering amplitude functions define the pattern and polarization of scattered electric field. The electric far field region is presented by,

$$\begin{pmatrix} E_{\parallel} \\ E_{\perp} \end{pmatrix}^{scat} = \frac{e^{-ikR+ikz}}{ikR} \cdot A_{scat} \cdot \begin{pmatrix} E_{\parallel} \\ E_{\perp} \end{pmatrix}^{inc} \tag{22}$$

where an incident plane wave is presented by e^{ikz}, the scattered light wave is $\frac{e^{-ikR}}{ikR}$, $R \gg kr_s^2$ is large distance at far field, $k = 2\pi/\lambda$ and parallel-perpendicular components of scattered and electric fields are denoted by $E_{\parallel}^{scat}$, $E_{\perp}^{scat}$ and $E_{\parallel}^{inc}$, $E_{\perp}^{inc}$ respectively. The unitless amplitude scattering matrix is represented by,

$$A_{scat} = \begin{bmatrix} S_2 & S_3 \\ S_4 & S_1 \end{bmatrix} \tag{23}$$

Considering spherical particles $S_a = S_4 = 0$, which deduces a fundamental equation of scattered radiation. The angle between incident electric field and scattering plane is represented by ϕ. The far field and orthogonal components are represented by,

$$E_{\parallel}^{scat} = \frac{e^{ikr_s}}{-ikr_s} cos(\phi) \cdot S_2[cos(\theta)] \tag{24}$$

$$E_{\perp}^{scat} = \frac{e^{ikr_s}}{ikr_s} sin(\phi) \cdot S_1[cos(\theta)] \tag{25}$$

It is observed that as the SiO_2 particle size increases, forward scattering becomes predominant in the same direction of the approaching light beam. On the other hand, very small amount of backward scattering is observed for the same situation. At some point, the extinction coefficient becomes a constant.

Therefore, regardless of the particle size relative to the wavelength, the scattering becomes uniform in the direction proportional to the intensity of the light. In addition, the angle and intensity of the scattered light depends on the particle size. From the observation made, larger particle scatters intensely at smaller angles. In contrary, smaller particles scatter light in a less intense manner at wider angles.

Forward, backward and side scattering of varying particle sizes, can be observed in Fig. 1. At incident wavelength of $\lambda_{nm} = 690$ nm, the main lobes exhibit peak forward scattering intensity for different particle radius at 6.08×10^{-5}, 39.63 and 408.2 respectively. The side lobes experience slightly-increased intensities of 0, 0.2269 and 0.3032. With increased r_s, non-polarized incident beam I_{Elip} predominantly excites the forward scattering process. Conversely, plane polarized beam I_{VV} is observed to be less interactive in particle-beam scattering scenario.

It is observed that, in terms of surface area, the large particles S_b to D_b have a ratio of 1:91.08. The reduced scattering coefficient $\mu_s'(\lambda)$ parameter exhibit wavelength impact on scattering behaviour. Prediction of scattering is observed with wavelength variation of λ = 350 nm-1500 nm for UV, visible and NIR range.

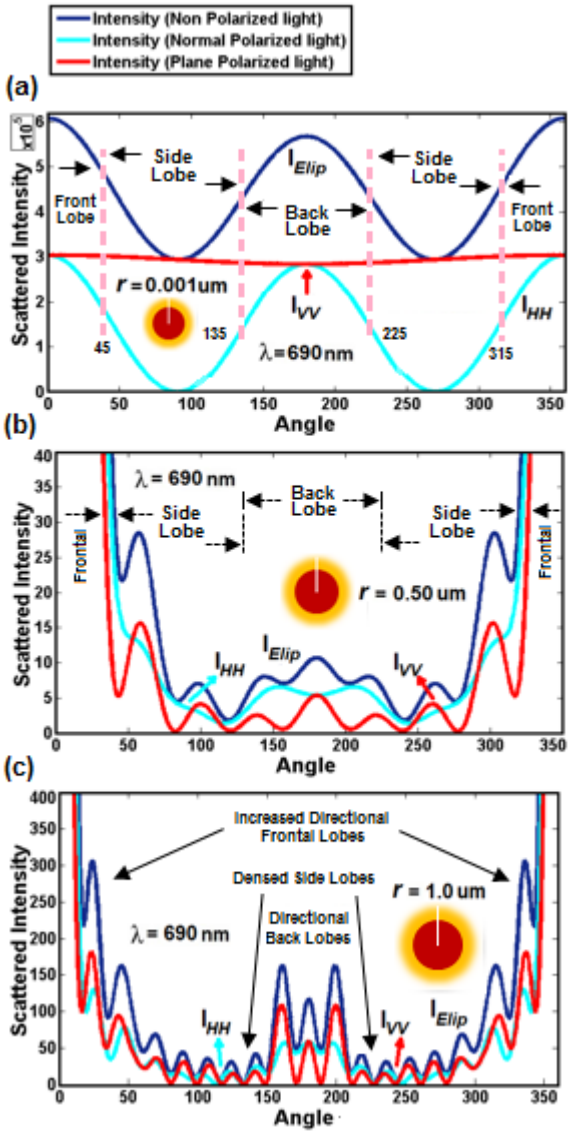

Fig. 1. Scattering properties of nanoparticle with granule radius at varying angular distribution. (a) Far-field scattering intensity simulation shows that light scattering is balanced along the backward and forward direction for structure with 1 nm core radius. Low scattering distribution is observed for I_{Elip} (plane polarization). (b) Scattering is wide and less directional with incident light at 532 nm and structure radius of 500 nm. (c) Non-polarization exhibit a strong directional forward and backward scattering for structure radius of 1 µm. Structures are irradiated respectively with different light source at λ = 470, 532 and 690 nm peak wavelength.

The μ_s' and μ_a optical properties govern the scattered light diffusion and reflectance of SiO_2 micro-nanoparticle, which can be observed by photodiode sensors. The theoretical analysis reveal the base $\mu_s'(\lambda)$ value at 0.16 x 10^{-5} when d

= 805 nm and concentration C = 1. It is observed in Fig. 2 that lower concentration and compact particle size contributes to decreasing $\mu_s'(\lambda)$ values.

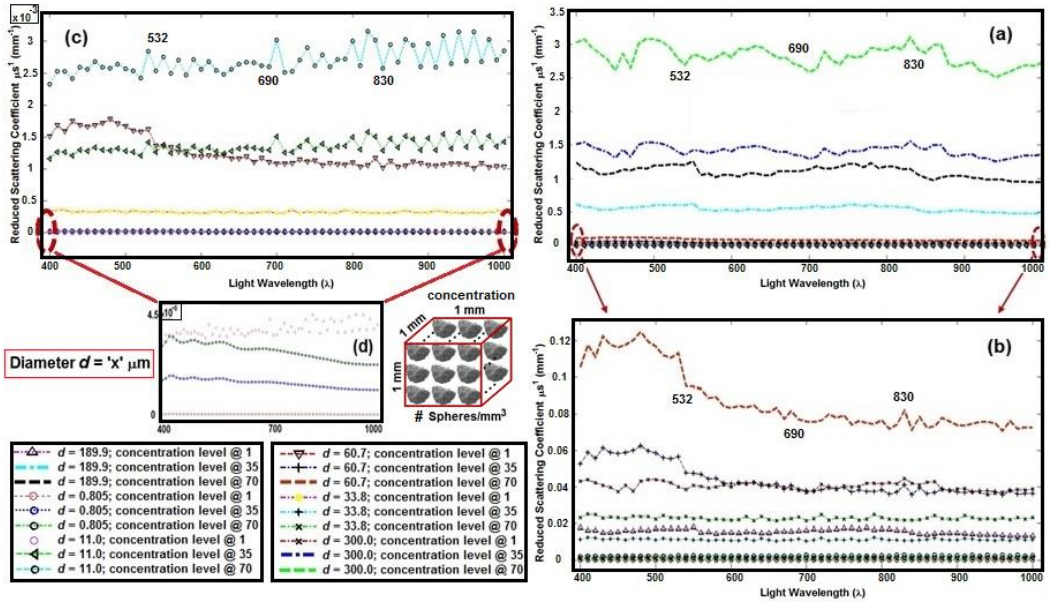

Fig. 2. Reduced scattering coefficient $\mu_s'(\lambda)$ measured as a function of the scattering angle λ (a) Theoretical behaviour of spherical SiO_2 nanostructures are observed in free space with structure core diameters d = 0.805, 11.0, 33.8, 60.7, 189.9 and 300.0 µm. (b) to (d) μ_s' decreases as the core size reduces with lower concentration C. The coefficients are calculated with Mie theory for 1, 35 and 70 spheres per 1 mm^3 respectively. At d = 0.805 µm and C = 1 sphere/mm^3, the lowest μ_s'= 3.2416 x 10^{-7} exhibits at λ = 1000 nm. For similar configuration, the theoretical peak reduced scattering μ_s'= 5.0525 x 10^{-7} is observed at λ = 470 nm. Rapid shifts in spectra can be detected by varying structure size and corresponding concentration level per 1 mm^3.

Wavelength specific single particle polar distribution is shown in Fig. 3(a) to 3(f). Theoretical measurements are investigated for extinction Q_{sca}, scattering Q_{ext} and backward dispersion Q_{bac}. It is observed that the extinction parameter Q_{sca} directively scatters in the forward direction as the particle size increases with particle size.

Wide distribution is observed at an incident wavelength $\lambda_{nm} = 830$ for d = 33.8 µm. The analysis indicates that the light dispersion process is intensely governed by colliding particle size and incident beam wavelength. The angular phase distribution of multiple core-shell SiO_2 micro-nanoparticle provides an insight to light-particle interaction in the context of dispersion efficiency.

Over the last two decades, numerous analyses are observed in the far field region of optical scattering and extinction cross-sections. On the contrary, studies on the near-field region for dielectric spheres are an emerging interest on optical scattering process. The scattering process of incident light beam on dielectric SiO_2 micro-nanoparticle generates complex patterns in the near field region. In geometrical optics viewpoint, the plane polarized incident wave and large 4 µm

dielectric SiO_2 sphere interaction in Fig. 4(c) creates a light converging impression of a convex lens. The intensifying scattering field with compact directional forward lobe manoeuvres such phenomena. It is reported by Hong Kong Observasary [28] that Mie scattering usually dictates as the particle size is observed to be larger than the incident wavelength $r_s \gg \lambda_{nm}$.

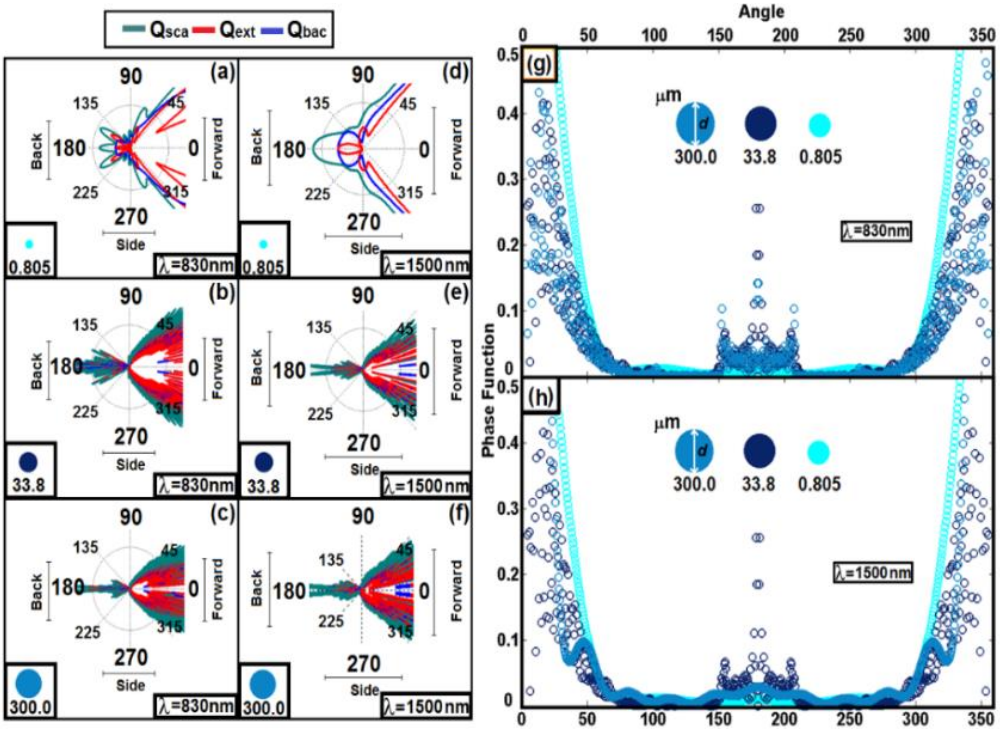

Fig. 3. Light scattering spectrum of core-shell SiO_2 nanoparticle with different particle size for wavelength-specific laser light source. (a-c) Scattering measurements (extinction, forward and backward) are investigated theoretically for near-infrared (NIR) light with particle core diameters of 0.805, 33.8 and 300.0 µm, respectively. (d-f) Similar measurements are observed to be directionally strong for infrared (IR) light. (g) The theoretical spectrum is calculated for three amorphous SiO_2 particles at λ = 830 nm. The bubble line (dark blue) indicates the peak forward scattering point at 5^0 and 355^0 angle. (h) Peak forward and backscattering is observed for dark blue bubble at angle 5^0, 355^0 and 181.5^0 respectively.

As shown in Fig. 4(a) to 4(c), the photonic nanojet effect is observed as Mie scattering paradigm yields intricate field distribution pattern reminiscent of directional antennas.

In free space, as the concentration of a fixed core-shell SiO_2 increase, the scattering coefficient is evidently observed to be slightly elevating. Stimulated by incident photons, the dynamic scattering coefficient describes the particle-containing medium at a fixed concentration C or volume density ρ_s. The theoretical base and peak scattering coefficient μ_s values can be observed in Fig. 5. The silica particle measurements for Fig. 5a-5c is obtained from the dust sample. Similarly,

Fig. 5(d) to 5(f) corresponding SiO_2 micro-nanoparticles are obtained from the construction site.

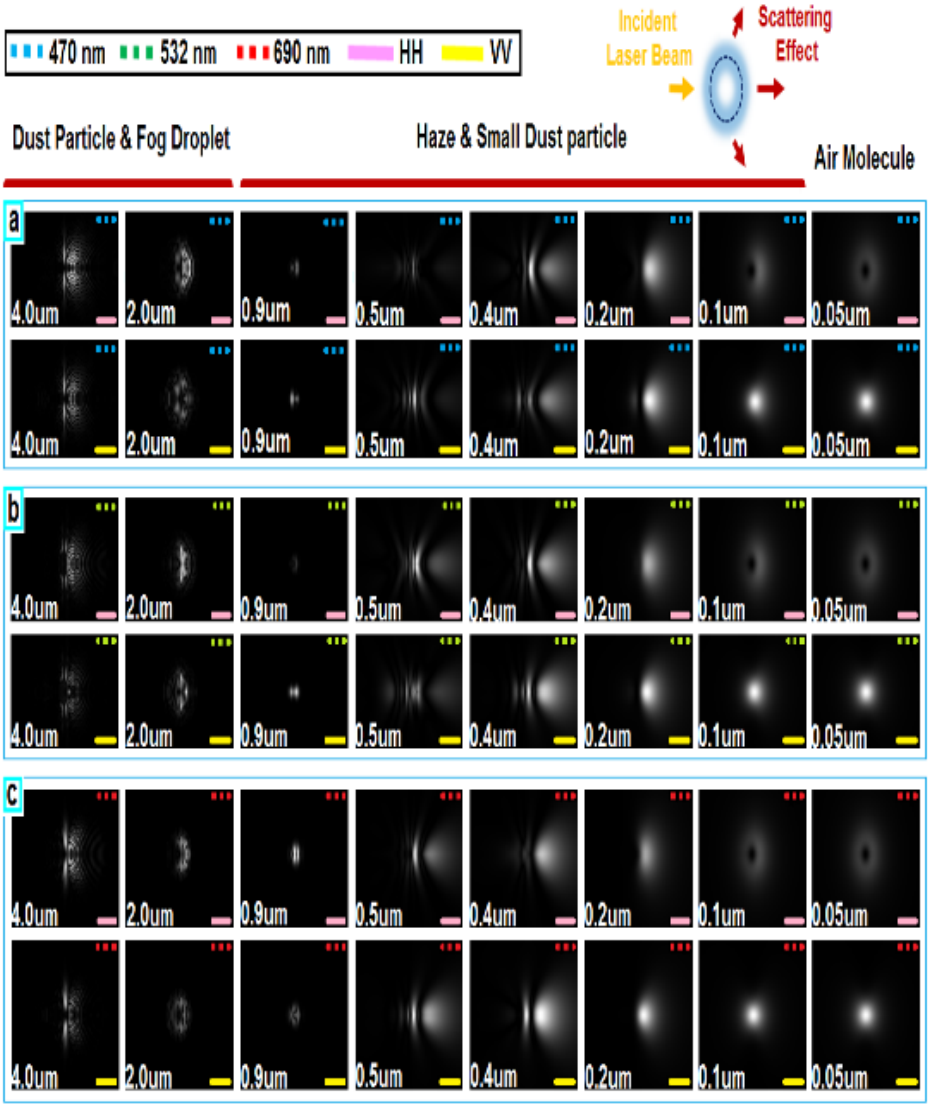

Fig. 4. Simulated illustrations for the scattered intensity of the spherical microparticles (variable radius r_n= 0.05 µm to 4.0 µm) when it is irradiated from left (see inset golden arrow) by a normal polarized (solid yellow line) or plane polarized (solid pink line) wave. (a) Minimum scattering condition at λ = 470 nm. (b) to (c) Medium and peak scattering intensities are observed for λ = 532 nm and 690 nm, respectively. (a) to (c) Calculated distribution of the total near-field intensity around the particle for different cases are considered for comparison purposes. At any given wavelength, as structure size increases, the scattering gets more intense in the forward direction.

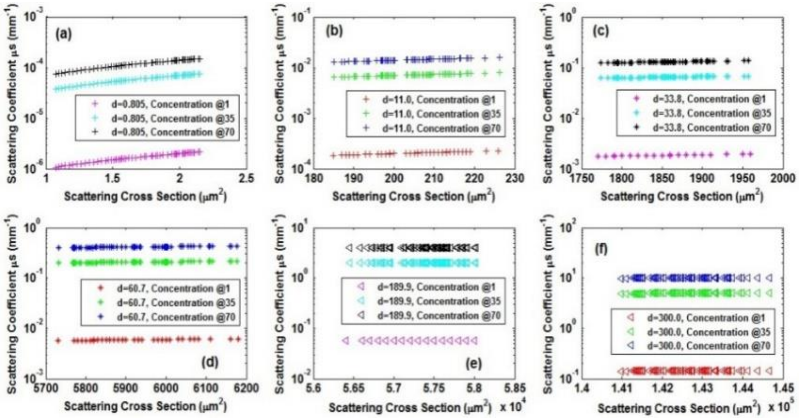

Fig. 5. Scattering coefficient μ_s elevates gradually as the concentration *C* of a spherical SiO_2 microparticle increases in free space. Structures with fixed core-shell diameters *d* exhibit slight escalation in μ_s as the scattering cross section area σ_{Scat} increases. (a) to (c) Theoretical behaviour of microparticle is observed for concentration *C* = 1, 35 and 70 sphere/mm^3. Structure configuration at *d* = 0.805 µm and *C* = 70, 1 sphere/mm^3, the peak and base coefficient μ_s is observed to be150.8 x 10^{-6} mm^{-1}, 10.13 mm^{-1} at σ_{Scat} = 2.155 µm^2, 14.47×10^4 µm^2, respectively. (d) to (f) Similar configuration for different particle diameter *d* = 300.0 µm, the theoretical peak and base scattering coefficient μ_s= 1.07×10^{-6} mm^{-1}, 0.141 mm^{-1} are observed at σ_{Scat} = 1.074 µm^2, 1.41 x 10^5 µm^2, respectively.

5. Results and Discussion

Scattering and absorption induced atmospheric attenuation is profoundly dependant on inbound beam wavelength and particle size parameter. Thus, efficiency of VLC will also be affected on the airborne atmospheric particles. It is reported by Weichel [22] that Kim model for visibility $v > 0.5$ indicates predominant wavelength dependency on atmospheric attenuation. Proposed Ijaz model evidently confirms a strong association between selective individual wavelength and measured data. Kim and Ijaz utilizes the visibility data to construct FSO link budget analysis. Likewise, proposed models in [16, 17, 22] considers the available visibility data instead of particle radius and Liquid Water Content (LWC). As a case analysis, we utilizes the proposed empirical models to observe atmospheric attenuation due to fog. The model verification indicates noticeable attenuation prediction against the measured data for very light fog, haze to clear atmospheric conditions. Take note that the proposed models can also be used to predict atmospheric attenuation due to dust and sand. Hong Kong Observatory (HKO) based measured visibility readings are collected from Chek Lap Kok, Central, Sai Wan Ho and Waglan Island [29]. The visibility meter based on hourly observations are composed for 5 days (6th November 2015 to 10th November 2015).

Visible 532 nm (green), 690 nm (red) and NIR 830 nm based laser beam is utilized with transmittance $\tau = 0.02$ as in Fig. 6(a) to 6(c) and $\tau = 0.05$ as in Fig. 6(d) to 6(f) to predict the atmospheric attenuation coefficient $\beta_\lambda(\upsilon)$. As shown in Fig. 6(d), atmospheric prediction for very light mist $\upsilon \cong 10$ km to clear air $\upsilon \cong 30$ km region indicates a considerable performance for Model 4. As the λ_{nm} increases, Model 1 indicates better fit. For the same configuration, visibility range of $1\ km \leq \upsilon \leq 4.5\ km$ (very light fog to very light mist) Model 2 demonstrates a decent fit against measured

data. On the contrary, analysis at $\upsilon \cong 1$km region delivers strong prediction for very light fog atmospheric conditions. At transmittance $\tau = 0.02$ and $\upsilon \cong 1$ km, the attenuation difference for 690 nm and 830 nm is observed with Proposed Model 1 to 3. Model 1 exhibits attenuation difference of 0.15 dB, while Model 2 and 3 indicate an increment for 0.67 dB and 0.82 dB, respectively. At $\lambda_{nm} = 690nm$, Model 2 predicted peak attenuation is observed at 16.08 dB. The base attenuation at 8.51 dB is induced by Model 3 at $\lambda_{nm} = 830\ nm$. In contrast, considering aeronautical transmittance at $\tau = 0.05$ and $\upsilon \cong 1\ km$, attenuation difference for Model 1 to 3 at 532 nm and 830 nm is observed at 0.39 dB, 1.32 dB and 1.72 dB, respectively. It is observed that a sudden rise in attenuation difference signifies the vital role of transmittance variable τ. As shown in Fig. 7(b), the Proposed Model 2 and 3 exhibits the peak and base attenuations of 13.12 dB and 6.89 dB at $\lambda_{nm} = 532\ nm$ and $\lambda_{nm} = 830\ nm$, respectively. It is reported by Bohren and Huffman [20] that the Kruse model was initially constructed for theoretical analysis of dense haze. At $\upsilon = 1$ km the model is considered incompatible to understand the fog attenuation behaviour. Conversely, for the visibility range of $0.5\ km \leq \upsilon \leq 1\ km$, Al-Naboulsi proposed a model for convection and advection fog effect analysis at a wavelength of 690 nm to 1550 nm. In contradiction to Kim's model for $\upsilon > 0.5$ km, Al-Naboulsi showed that the fog attenuation is higher for 1550 nm compared to 785 nm. Further study on empirical data in region $\upsilon < 1$ km indicated that β_λ is wavelength independent for $\upsilon < 0.5$ km. This led to controversial μ values of Kim model. This model in comparison to Al-Naboulsi advection and convection fog models exhibit lower fog attenuation.

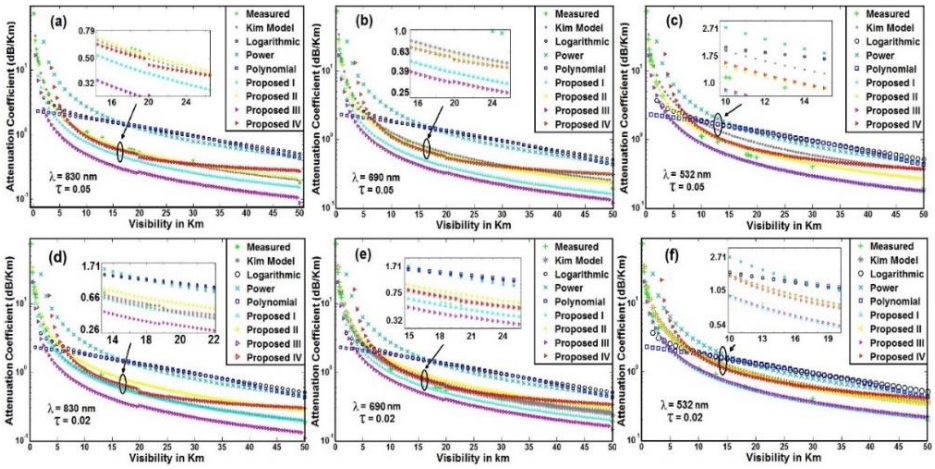

Fig. 6. Atmospheric optical attenuation $\beta_\lambda(v)$ is observed as a function of visible waveband under various weather conditions. Several models exhibit close prediction against the measured data. (a) to (c) The aeronautical requirements sets the transmittance threshold τ at 5%. At increasing visibility v = 1 km to 20 km, optimal absolute residual value |R| is observed to be 0.068 and 0.108 for different incident light wavelength λ = 830 nm and 532 nm, respectively. (d-f) Considering Koschmieder law, the transmittance threshold τ is set to 2%. |R|is observed at 0.0478 for λ = 690 nm. Proposed 1 model is found to be an optimal fit for both transmittance threshold driven scenario. The light source is a laser transmitter with wavelength set to λ = 830 nm, 690 nm and 532 nm, respectively.

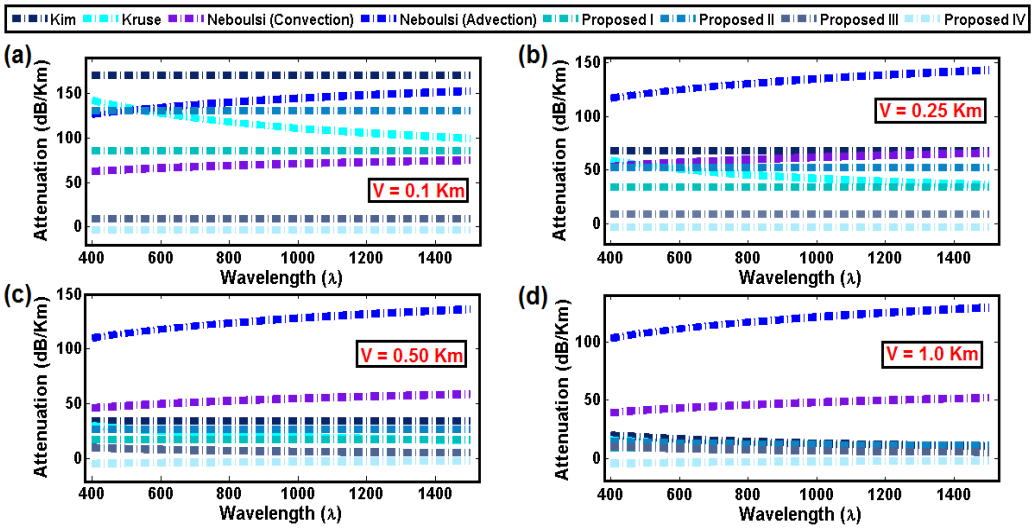

Fig. 7. Comparison of proposed and existing empirical models for a range of wavelengths λ_{nm} with different visibility v values (a) 100 m, (b) 250 m, (c) 500 m and (d) 1000 m.

Error estimation for all models in very light fog to clear air condition ($1\ km \leq v \leq 20\ km$) is presented in Table 2 to Table 5. Different transmittance conditions for optical signal attenuation at $\lambda_{nm} = 830$ nm can be observed from Table 3 and Table 4. The model specific μ values play an important role in performance measurement. The error estimation RMSE values are determined by comparing each model against the measured data. The proposed models exhibit promising performance for very light mist to clear air region. For the same region, proposed Model 4 exhibits the best fit at 0.015. For very light mist region (4 km $\leq v \leq$ 10 km), apart from curve fitting power model (RMSE = 1.375), the Model 3 (RMSE = 0.570) error rate is observed to be relatively high for wavelength $\lambda_{nm} = 830$ nm with transmittance threshold at $\tau = 0.02$. However, it is understood that the models are not capable of providing solution to mixed fog-mist weather conditions. On this note, it is observed that mixed case of very light fog to light mist region shows poor model prediction performance.

Table 2. Error estimation of attenuation models in various weather constituents for λ = 830 nm and transmittance threshold τ at 0.05.

	Very light fog/light mist (1,000-4,000 m)			Very light mist (4,000-10,000 m)			Clear air/drizzle (18,100-20,000 m)		
Model	μ	R^2	**RMSE**	μ	R^2	**RMSE**	μ	R^2	**RMSE**
Proposed 1	1.30	17.882	4.229	0.18	0.109	0.331	0	0.029	0.171
Proposed 2	1.30	2.416	1.554	0.41	0.010	0.098	0.05	0.001	0.029
Proposed 3	1.15	27.527	5.247	0	0.325	0.570	0	0.100	0.317
Proposed 4	n/a	n/a	n/a	0.32	0.036	0.189	0.01	0.004	0.065
Kim model	1.30	0.049	0.220	0.38	0.017	0.130	0.03	0.002	0.049
Polynomial	n/a	68.54	8.279	n/a	0.525	0.725	n/a	n/a	n/a
Power model	n/a	n/a	n/a	n/a	1.890	1.375	n/a	n/a	n/a
Logarithmic	n/a	n/a	n/a	n/a	0.598	0.773	n/a	n/a	n/a

Table 3. Error estimation of attenuation models in various weather constituents for λ = 532 nm and transmittance threshold τ at 0.05.

	Very light fog/light mist (1,000-4,000 m)			Very light mist (4,000-10,000 m)			Clear air/drizzle (18,100-20,000 m)		
Model	**μ**	**R^2**	**RMSE**	**μ**	**R^2**	**RMSE**	**μ**	**R^2**	**RMSE**
Proposed 1	1.30	15.203	3.899	0.26	0.063	0.251	0	0.015	0.123
Proposed 2	1.30	0.235	0.484	0.53	0.032	0.179	0.21	0.017	0.130
Proposed 3	1.15	14.491	3.807	0.28	0.051	0.226	0	0.012	0.108
Proposed 4	n/a	n/a	n/a	0.54	0.067	0.258	0.24	0.025	0.159
Kim model	1.30	7.096	2.664	0.59	0.327	0.572	0.46	0.134	0.366
Polynomial	n/a	68.54	8.28	n/a	0.525	0.725	n/a	n/a	n/a
Power model	n/a	n/a	n/a	n/a	n/a	n/a	n/a	n/a	n/a
Logarithmic	n/a	n/a	n/a	n/a	0.598	0.773	n/a	n/a	n/a

Table 4. Error estimation of attenuation models in various weather constituents for λ = 830 nm at transmittance threshold τ at 0.02.

	Very light fog/light mist (1,000-4,000 m)			Very light mist (4,000-10,000 m)			Clear air/drizzle (18,100-20,000 m)		
Model	**μ**	**R^2**	**RMSE**	**μ**	**R^2**	**RMSE**	**μ**	**R^2**	**RMSE**
Proposed 1	1.30	7.528	2.744	0.35	0.024	0.156	0.010	0.004	0.065
Proposed 2	1.30	1.305	1.143	0.53	0.038	0.194	0.220	0.019	0.139
Proposed 3	1.15	16.676	4.084	0.04	0.218	0.466	0	0.064	**0.253**
Proposed 4	n/a	n/a	n/a	0.47	0.003	**0.059**	0.090	0.0002	**0.015**
Kim model	1.15	0.048	**0.220**	0.38	0.017	0.129	0.030	0.002	0.049
Polynomial	n/a	68.548	**8.279**	n/a	n/a	n/a	n/a	n/a	n/a
Power model	n/a	n/a	n/a	n/a	1.890	**1.374**	n/a	n/a	n/a
Logarithmic	n/a	n/a	n/a	n/a	0.598	0.773	n/a	n/a	n/a

Table 5. Error estimation of attenuation models in various weather constituents for λ = 690 nm and transmittance threshold τ at 0.02.

	Very light fog/light mist (1,000-4,000 m)			Very light mist (4,000-10,000 m)			Clear air/drizzle (18,100-20,000 m)		
Model	**μ**	**R^2**	**RMSE**	**μ**	**R^2**	**RMSE**	**μ**	**R^2**	**RMSE**
Proposed 1	1.30	6.870	2.621	0.380	0.017	0.129	0.031	0.002	**0.049**
Proposed 2	1.30	2.773	1.665	0.549	0.098	0.313	0.291	0.044	**0.211**
Proposed 3	1.15	11.528	3.395	0.188	0.102	0.319	0	0.027	0.164
Proposed 4	n/a	n/a	n/a	0.525	0.029	0.170	0.191	0.012	0.112
Kim model	1.30	0.986	**0.993**	0.519	0.015	**0.124**	0.175	0.009	0.095
Polynomial	n/a	68.548	**8.279**	n/a	0.525	0.724	n/a	n/a	n/a
Power model	n/a	n/a	n/a	n/a	1.890	**1.375**	n/a	n/a	n/a
Logarithmic	n/a	n/a	n/a	n/a	0.598	0.773	n/a	n/a	n/a

Dense, moderate to very light fog attenuation models for $0.4\mu m \leq \lambda_{nm} \leq 1.5\ \mu m$ and υ = 0.1, 0.25, 0.5 and 1.0 km are presented in Figs. 7(a) to 7(d). The theoretical analysis shows the correlation for a range of $0.5\mu m \leq \lambda_{nm} \leq 1.4\mu m$ and υ = 1 km. According to Grabner and Kvicera [29], Kim, Kruse, Naboulsi (advection) and Naboulsi (convection) empirical models are verified against the experimental

data to indicate a prominent correlation. Theoretical observation reveals that Kim and Kruse models exhibit similar performance for estimating fog attenuation in $0.5\mu m \leq \lambda_{nm} \leq 1.4\ \mu m$ region.

Likewise, proposed Model 2 demonstrates identical behavior for the similar configuration. At υ = 1 km, a two-sided intersecting bound is identified where left and right bound is observed at $550\ nm \leq \lambda_{nm}$) and $\lambda_{nm} \leq 1400\ nm$, respectively. Crisscrossing Kruse and Model 2 displays left and right bound attenuation of 13.01 dB and 10.58 dB. At the edge of right bound, decreasing Model 2 is observed to intersect Kim. On the contrary, Model I exhibits close prediction against Kruse model on a wavelength window of $1.1\ \mu m \leq \lambda_{nm} \leq 1.4\ \mu m$. The peak prediction for Kruse and Model 1 on this window is observed to be 8.68 dB and 7.89 dB at 1.1 µm. The same models exhibit base power of 7.73 dB and 7.53 dB at 1.4 µm. The detailed theoretical analysis supports the fact that proposed Model 2 is an ideal alternative for predicting dense to very light fog attenuation.

6. Conclusion

In this paper, we have proposed few new empirical models to predict the atmospheric attenuation that can be affected by the presence of airborne microparticle such as sand, fog and smoke like particle movement. We compare of those with existing models for verification purpose of best fitting models for attenuation. Thorough analysis and comparisons at different range of visibility suggested that the proposed models exhibit better overall performance than the existing models. In order to achieve best attenuation prediction, it is suggested that different proposed models should be used accordingly depending on the visibility range. However, it must be noted that proposed Model 2 best suited for predicting dense to very light fog attenuation. As far as future work is concerned, more experimental work will be carried out to validate the empirical models under various weather conditions.

Nomenclatures

$Abs_{mol}(\lambda)$	Molecular absorption
$Abs_{Aeo}(\lambda)$	Aerosol absorption
d	Diameter
I_O	Intensity
L_T	Transmission path length
P_{Abs}	Absorbed electromagnetic energy across an imaginary surface of sphere
P_R	Optical power at receiver
P_{Scat}	Scattered electromagnetic energy across an imaginary surface of sphere
P_T	Transmitted power
Q_{Scat}	Theoretical normalized scattering efficiency
r	Radius
$Scat_{Aeo}(\lambda)$	Aerosol scattering coefficients
$Scat_{mol}(\lambda)$	Molecular scattering coefficients
$T_O(\lambda, L_T)$	Total optical transmittance
T_{th}	Transmittance threshold

Greek Symbols

α	Parameters characterize the structural size distribution
β	Parameters characterize the structural size distribution
$\beta_A(\lambda)$	General atmospheric attenuation coefficient
$\beta_\lambda(\upsilon)$	Atmospheric attenuation coefficient
$\gamma(\upsilon)$	Optical power
$\boldsymbol{\lambda}$	Wavelength
μ	Particle size related coefficient
τ_{Od}	Optical depth
υ	Meteorological visibility
ϕ_{xx}	Angle between incident electric field and scattering plane

Abbreviations

FSO	Free Space Optics
IR	Infra-Red
LED	Light Emitting Diodes
NOAA	National Oceanic and Atmospheric Administration
OWC	Optical Wireless Communication
RF	Radio Frequency
VLC	Visible Light Communication

References

1. O'Brien, D.C.; Faulkner, G.E.; Jim K.; Zyambo, E.B.; Edwards, D.J.; Whitehead; M.; Stavrinou, P.; Parry, G.; Bellon, J.; Sibley, M.J.; Lalitambika, V.A.; Joyner, V.M.; Shamsudin, R.J.; Holburn, D.M.; and Mears R.J. High-speed integrated transceivers for optical wireless. *IEEE Communication Magazine*, 41(3), 58-62.
2. Salian, P.P.; Prabhu, S.; Amin, P.; Naik, S.K.; and Parashuram, M.K. (2013). Visible light communication. *Proceedings of Texas Instruments India Educators Conference. Bangalore, Karnataka, India*, 379-383.
3. Giustiniano, D.; Tippenhauer, N.O.; and Mangold, S. (2012). Low-complexity visible light networking with LED-to-LED communication. *Proceedings of the IFIP Wireless Days*. Dublin, Ireland, 1-8.
4. Minh, H.L.; Ghassemlooy, Z.; O'Brien, D.; and Faulkner, G. (2010). Indoor gigabit optical wireless communications: Challenges and possibilities. *Proceedings of the 12th International Conference on Transparent Optical Networks*. Munich, Germany, 1-6.
5. Langer, K.-D.; Grubor, J.; Bouchet, O.; El Tabach, M.; Waleski, J.W.; Randel, S.; Franke, M.; Nerreter, S.; O'Brien, D.C.; Falkner, G.E.; Neokosmidis, I.; Ntogari, G.; and Wolf, M. (2008). Optical wireless communications for broadband access in home area networks. *Proceedings of 10th Anniversary International Conference on Transparent Optical Networks*. Athens, Greece, 149-154.
6. Harb, K.; Omair, B.; Abdul-Jauwad, S.;. Al-Yami, A.; and Al-Yami, A. (2012). A proposed method for dust and sand storms effect on satellite communication networks. *Proceedings of Innovations on Communication Theory*. Istanbul, Turkey, 33-37.

7. Harb, K.; Butt, O.; Abdul-Jauwad, S.; and Al-Yami, A.M. (2013). Systems adaptation for satellite signal under dust, sand and gaseous attenuations. *Journal of Wireless Networking and Communications*, 3(3), 39-49.
8. Alhaider, M.A. (1986). Radio wave propagation into sandstorms-system design based on ten-years visibility data in Riyadh, *Saudi Arabia. International Journal of Infrared and Millimeter Waves*, 7(9), 1339-1359.
9. Ijaz, M.; Ghassemlooy, Z.; Minh, H.L.; Rajbhandari, S.; and Perez, J. (2012). Analysis of fog and smoke attenuation in a free space optical communication link under controlled laboratory conditions. *Proceedings of the International Workshop on Optical Wireless Communications*. Pisa, Italy, 1-3.
10. Perez, J.; Ghassemlooy, Z.; Rajbhandari, S.; Ijaz, M.; and Minh, H.L. (2012). Ethernet FSO communications link performance study under a controlled fog environment. *IEEE Communications Letters*, 16(3), 408-410.
11. Mahalati, R.N.; and Kahn, J.M. (2012). Effect of fog on free-space optical links employing imaging receivers. *Journal of Optics Express*, 20(2), 1649-1661.
12. Chowdhury, A.K.; and Reaz, M.B.I (2016). Performance analysis of wavelength specific transmission in turbulent medium for free space optical communication systems. *Proceedings of the International Conference on Advances in Electrical, Electronic and Systems Engineering*. Putrajaya, Malaysia, 535-538.
13. Kim, M-D.; Liang, J.; Lee, J.; Park, J.; and Park, B. (2016). Path loss mesurements and modeling for indoor office scenario at 28 and 38 GHz. *Proceedings of the International Symposium on Antennas and Propagation.* Okinawa, Japan, 64-65.
14. Sulyman, A.I.; Alwarafy, A.; MacCartney, G.R.; and Rapport, T.S. (2016). Directional radio propagation path loss models for millimiter-wave wireless networks in the 28-, 60-, and 73- GHz bands. *IEEE Transactions on Wireless Communications*, 15(10), 6939-6947.
15. Kok, J.F.; Parteli, E.J.R.; Michaels, T.I.; and Karam, D.B. (2012). The physics of wind-blown sand and dust. *Reports on Progress in Physiscs*, 75(10), Article No. 106901.
16. Shao, Y. (2008). *Physics and modelling of wind erosion* (2nd ed.). Heidelberg, Germany: Springer Science and Business Media B.V.
17. Email, I.W.; Sani, N.A.; Abdulsalam, A.K.; and Abdullahi, U.A. (2013). Extraction and quantification of silicon from silica sand obtained from Zauma River, Zamfara State, Nigeria. *European Scientific Journal*, 9(15), 160-168.
18. Willebrand, H.; and Ghuman, B.S. (2002). *Free space optics: Enabling optical connectivity in today's network*. Indianapolis: Sams Publishing.
19. Ghassemlooy, Z.; Popoola, W.; and Rajbhandari, S. (2013). *Optical wireless communications: System and channel modelling with MATLAB*. Boca Raton, Florida: CRC Press.
20. Bohren, C.F.; and Huffman, D.R. (1983). *Absorption and scattering of* light *by small particles*. New York: John Wiley and Sons, Inc.
21. Ijaz, M.; Gaseemlooy, Z.; Pesek, J.; Fiser, O.; Minh, H.L.; and Bently, E. (2013). Modelling of fog and smoke attenuation in free space optical communication link under controlled laboratory conditions. *Journal of Lightwave Technology*, 31(11), 1720-1726.

22. Weichel, H. (1990). *Laser beam propagation in the atmosphere*. Washington: SPIE Press.
23. Kruse, P.W.; Mcglauchin, L.D; and Mcquistan, R.B. (1962). *Elements of Infrared technology: Generation, transmission and detection*. New York: Wiley: John Wiley and Sons, Inc.
24. Grabner, M.; and Kvicera, V. (2012). The wavelength dependant model of extinction in fog and haze for free space optical communication. *Optics Express*, 19(4), 3379-3386.
25. Kim, I.I.; Mcarthur, B.; and Korevaar, E.J. (2001). Comparison of laser beam propagation at 785 nm and 1550 nm in fog and haze for optical wireless communications. *Proceedings of SPIE 4214 Optical Wireless Communication*. Boston, United States of America, 12 pages.
26. Duvey, D.; and Gupta, E.R. (2014). Analysis of fog attenation models for multitransceiver FSO system for different frequencies. *International Journal of Application or Innovation in Engineering & Management*, 3(6), 216-220.
27. Fan, X.; Zheng, W.; and Singh, D.J. (2014). Light scattering and surface plasmons on small spherical particles. *Light: Science & Applications*, 3, 38 pages.
28. Hong Kong Observasary (2012). Visibility readings in hong kong waters. Retrieved January 3, 2017, from https://www.hko.gov.hk/vis/vis_ textonly_e.shtml?Seltime=201810282400.
29. Grabner, M.; and Kvicera, V. (2010). Case study of fog attenuation on 830 nm and 1550 nm freespace optical links. *Proceedings of the Fourth European Conference on Antennas and Propagation (EuCAP)*. Barcelona, Spain, 1-4.